IEEE Access
Multidisciplinary ⋮ Rapid Review ⋮ Open Access Journal

Received 17 February 2023, accepted 24 April 2023, date of publication 27 April 2023, date of current version 4 May 2023.

Digital Object Identifier 10.1109/ACCESS.2023.3270900

RESEARCH ARTICLE

PNCS: Pixel-Level Non-Local Method Based Compressed Sensing Undersampled MRI Image Reconstruction

HAO HOU[1,2], YUCHEN SHAO[3], YANG GENG[2], YINGKUN HOU[4], (Senior Member, IEEE), PENG DING[1,5], AND BENZHENG WEI[2]

[1]College of Intelligence and Information Engineering, Shandong University of Traditional Chinese Medicine, Jinan 250355, China
[2]Qingdao Academy of Chinese Medical Sciences, Shandong University of Traditional Chinese Medicine, Qingdao 266112, China
[3]School of Computer Science and Technology, Shandong University, Qingdao 266237, China
[4]School of Information Science and Technology, Taishan University, Tai'an 271000, China
[5]Information Center, The Second Affiliated Hospital of Shandong University of Traditional Chinese Medicine, Jinan 250001, China

Corresponding authors: Peng Ding (dpabc@163.com) and Benzheng Wei (wbz99@sina.com)

This work was supported in part by the National Natural Science Foundation of China under Grant 61872225 and Grant 62071320; in part by the Natural Science Foundation of Shandong Province under Grant ZR2020MF038, Grant ZR2020KF013, Grant ZR2020ZD44, Grant ZR2019ZD04, and Grant ZR2020QF043; in part by the Science and Technology Innovation Development Project of Tai'an City under Grant 2020GX028 and Grant 2021GX045; in part by the Shandong Province Science and Technology Small and Medium-size Enterprise (SMEs) Innovation Capacity Improvement Project under Grant 2022TSGC2195; and in part by the Introduction and Cultivation Program for Young Creative Talents in Colleges and Universities of Shandong Province under Grant 2019-173.

ABSTRACT Compressed sensing magnetic resonance imaging (CS-MRI) has made great progress in speeding up MRI imaging. The existing non-local self-similarity (NSS) prior based CS-MRI models mainly take similar image patches as the processing objects, this patch-level non-local sparse representation method can not make full use of the self-similarity among pixels in the image, so it can not recover the weak edge information in the undersampled MRI image well and there will still be some artifacts. In this paper, a pixel-level non-local method based compressed sensing undersampled MRI image reconstruction method is introduced. First, zero filling is performed on the undersampled k-space data to obtain a full-size 2D signal, and IFFT is performed to obtain a preliminary reconstructed MRI image. Block-matching and row-matching are successively performed on the reconstructed image in turn to obtain similar pixel groups, so as to establish a better sparse representation under the non-local self-similarity (NSS) prior. The separable Haar transform is performed on similar pixel groups, and the hard threshold of the transform coefficients and Wiener filtering can effectively remove the artifacts introduced in the undersampled reconstructed MRI images. The proposed pixel-level non-local iterative thinning model based on compressed sensing theory can ensure the removal of artifacts and better restore the details in the image. The qualitative and quantitative results under different undersampling modes and undersampling rates prove the advantages of the proposed method in subjective visual quality and objective evaluation (peak signal to noise ratio and structure similarity index). The performance of this method is not only superior to the existing traditional CS-MRI methods, but also competitive with the existing deep neural network (DNN) based models. The code will be released at https://github.com/HaoHou-98/PNCS.

INDEX TERMS Pixel-level non-local, compressed sensing, undersampled MRI image reconstruction.

I. INTRODUCTION

Magnetic resonance imaging (MRI) is a widely used medical clinical imaging modality. However, it is usually limited in the imaging speed by its k-space (i.e., Fourier space) acquisition data mode. In the early stages, some accelerated techniques such as fast sequence-based algorithms [1], [2], [3], [4] and parallel imaging (PMRI)-based algorithms [5], [6] must utilize full k-space coverage that satisfies the Nyquist-Shannon sampling criterion. However, the above full

The associate editor coordinating the review of this manuscript and approving it for publication was Barbara Masucci.

sampling methods depend more on the quantity and performance of the acquisition coils, showing limited potential for accelerating MRI. Directly reducing the sampling rate can significantly speed up imaging, however, reduction of the sampling rate inevitably introduces aliasing artifacts in the reconstructed images, which significantly affects the diagnosis of the doctors. Thus, a widely studied problem is how to reconstruct MRI images from undersampled k-space data that preserves as much information as possible from fully-sampled data.

In the past two decades, the compressed sensing theory has provided strong technical support for the accelerated reconstruction of MRI image. In the CS theory, sparsity is a prerequisite for reconstructing undersampled signals [7]. Existing CS-MRI methods usually explore the sparse representation in a specific transform domain, such as total variation (TV) [8], [9], [10], discrete wavelet transform (DWT) [11], [12], [13], and discrete cosine transform (DCT) [14], [15], [16], etc. Additionally, sparse representation can be learned directly from the data using dictionary learning [17], [18], [19]. Once the desired sparse representation matrix is obtained, a nonlinear optimization algorithm can be used to obtain better reconstruction results [7], [9], [20], [21]. However, the above-mentioned conventional CS-MRI methods are usually difficult to capture complex image details using predefined or fixed sparse transformations, e.g., the TV-based methods may introduce staircase artifacts [22], and the wavelet transform-based methods may introduce ring artifacts [23]. To alleviate the above problems, some dictionary learning-based methods [17], [18], [19] learn sparse representation directly from the data. Besides, [24] proposed using the NSS prior to image patches to construct sparse transformation, nevertheless, the patch-level NSS methods still cannot achieve satisfactory results in the reconstruction process of contour or texture regions.

Recently, the powerful deep neural networks (DNNs) have also been widely used in CS-MRI [23], [25], [26], [27], [28], [29], [30], [31], [32], [33]. According to the learning method, DNN-based CS-MRI models can be roughly divided into supervised [23], [25], [26], [27], [28], [29] and unsupervised [30], [31], [32], [33] learning models. Among supervised learning models, the initial deep end-to-end (ETE) models introduced the image segmentation model U-Net [34] to the task of undersampled MRI image reconstruction and achieved promising performance. Later, the self-attention mechanism was adopted to obtain higher visual quality reconstruction results [27]. However, the ETE models usually require large sample sizes to train networks. In addition, some supervised models based on Unrolled Optimization (UO) [26], [28] try to combine DNNs with traditional iterative-based CS algorithms to constrain image reconstruction by learning regularization methods, however, its iterative reconstruction method requires more computation time [35]. The supervised learning models usually require large amounts of paired data to establish a mapping between the undersampled to fully sampled image domains, however, the paired data is challenging to obtain in the real world, if not impossible. To alleviate this problem, unsupervised learning models [30], [31], [32], [33], which proposed a new solution using UO and alternately optimizing reconstructed images and model parameters, have achieved impressive performance. However, whether it is a supervised or unsupervised model, they are usually more limited in generalization ability than conventional CS-MRI methods, and they may not adequately consider the sparsity of the data.

In this paper, pixel-level NSS prior [36] to CS-MRI is introduced. Compared with previous patch-based NSS priors, the self-similarity among pixels is beneficial to constructing better sparse transformations. Besides, we design a pixel-level non-local refinement model to utilize pixel-level NSS prior to an iteratively refined model and reconstruct undersampled MRI images. The proposed model can achieve satisfactory undersampled MRI image reconstruction results, both objective evaluation and subjective visual quality are better than existing methods.

II. METHODS

A. BACKGROUND OF CS-MRI

The approximate discrete linear system of the observation model for undersampled MRI image reconstruction is as the following:

$$y = Ux + \varepsilon \tag{1}$$

where $x \in \mathbb{C}^N$ represents the desired k-space data which needs to be recovered, $U \in \mathbb{C}^{M\times N}(M \ll N)$ is the compressed sensing matrix. For compressed sensing MRI, U can be the undersampling operation on x (Fourier transform spectrum of the MRI image) in various undersampling modes [7], $y \in \mathbb{C}^M$ is the actual undersampled k-space data, and $\varepsilon \in \mathbb{C}^M$ is the error between undersampled Fourier spectrum and the Fourier spectrum of reconstructed image. The classic CS-MRI reconstruction attempts to solve the following problem [7]:

$$\hat{x} = \arg\min_x \left\{ \|\psi^T x\|_1 + \frac{\lambda}{2}\|y - Ux\|_2^2 \right\} \tag{2}$$

where ψ^T is a sparsity transform of x, $\|\cdot\|_1$ being the ℓ_1-norm is used to represent the sparsity of $\psi^T x$ in compressed sensing theory, and $\|\cdot\|_2$ is the ℓ_2-norm which enforces the fidelity of the reconstruction to the measured k-space data. The regularization parameter λ determines the trade-off between the sparsity and the data fidelity.

From a Bayesian perspective, sparsity prior is of central importance for CS-MRI. The existing CS-MRI methods are more likely to use predefined sparse transformations to represent images sparsely. However, the reconstruction results of these methods always introduce too many artifacts. To alleviate this problem, PANO [24] attempts to exploit patch-based

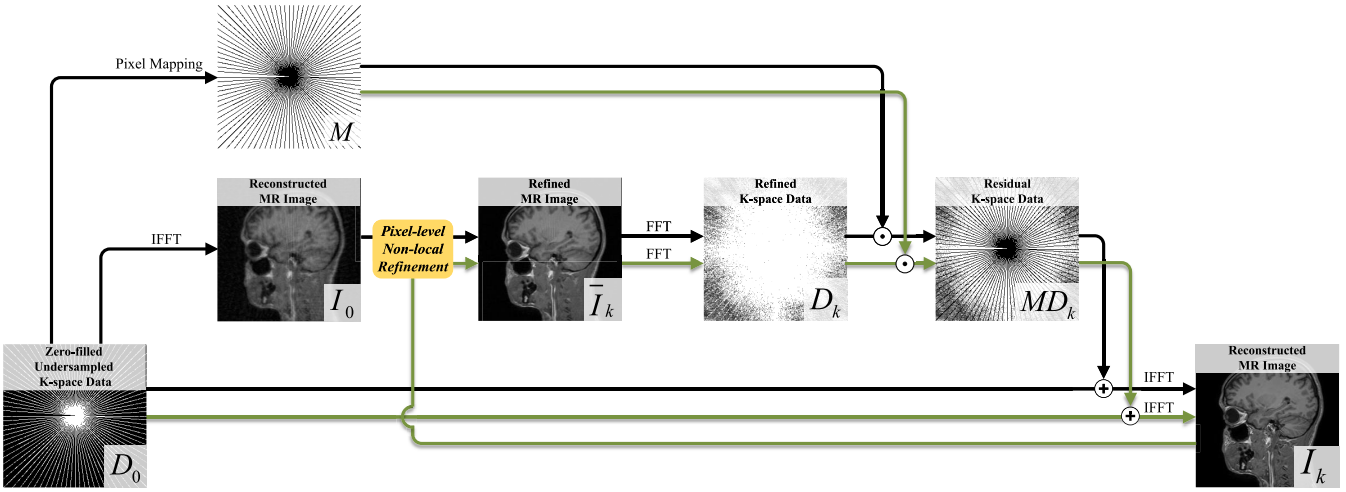

FIGURE 1. Flowchart of the proposed PNCS iteration refinement undersampled k-space data reconstruction. Where k ($k = 1, \cdots, \mathrm{K}$) means the k-th step iteration. The black line in the figure represents the initial step, the green line represents the iteration procedure.

non-local self-similarity priors to construct sparse transformations, however, it tends to introduce artifacts on the contour/texture of the reconstruction results. To fully capture the self-similarity of pixels in an image, we go one step further to introduce a pixel-level self-similar prior to CS-MRI. We have constructed a better sparse transformation and achieved better performance than existing CS-MRI methods.

B. PIXEL-LEVEL NON-LOCAL ITERATION REFINEMENT MODEL

1) OVERVIEW

Given an undersampled k-space data $D_u \in \mathbb{C}^M$, as suggested in [24], we use zero-filling as a pre-processing to complete data, and get a full size 2-D k-space data $D_0 \in \mathbb{C}^{\sqrt{N}\times\sqrt{N}}$. As shown in Fig 1, we implement preliminary reconstruction on the zero-filled k-space data D_0 by inverse fast Fourier transform (IFFT), thus obtain a preliminary reconstructed MRI image I_0, which usually introduce strong aliasing artifacts. Once we obtained I_0, we perform *pixel-level non-local refinement* (the detailed implementation will be introduced in §II-B2) to obtain the refined MRI image $\overline{I}_k$ ($k \in 1, \cdots, \mathrm{K}$), which can restore the undersampled signal and eliminate artifacts, as well as ensure the sparsity (the ℓ_1-norm part in Eq. 2). Then $\overline{I}_k$ is transformed to k-space data D_k by fast Fourier transform (FFT).

We always supplement the restored data by the k-th iteration D_k to the zero-filled position of k-space D_0, which is to maintain the fidelity of the really sampled data (i.e. minimize the ℓ_2-norm part in Eq. 2). For this purpose, we generate a map M according to the zero-filled undersampled k-space data D_0 by the following mapping function f:

$$f = \begin{cases} 0, & v \neq 0; \\ 1, & v = 0. \end{cases} \tag{3}$$

where v is the element value of the original undersampled k-space data D_0.

In each step iteration, we use a dot product between the refined k-space data D_k and the map M to obtain the desired residual k-space data MD_k, and add the residual to the original undersampled k-space data D_0. Finally, we implement IFFT to obtain the reconstructed image I_k which will be used as the input of the next iteration.

2) PIXEL-LEVEL NON-LOCAL REFINEMENT

The proposed pixel-level non-local refinement model includes the following four steps: *1) Patch-matching*, *2) Row-matching*, *3) Bi-Hard Thresholding-Based Basic Refinement*, and *4) Improved Wiener Filtering-Based Final Refinement*. The detailed implementations are described below.

a: PATCH-MATCHING

As shown in Figure 2, we implement patch-matching to obtain a certain number of similar patches in a given undersampled reconstruction MRI image $x \in \mathbb{R}^{h\times w}$. A reference image patch B_r with the size of $\sqrt{n} \times \sqrt{n}$ in the image according to a given sliding step size is selected (We assume that there are N reference image patches are selected, the number of reference patches approximately equals to $\frac{hw}{step^2}$). We implement patch-matching by Euclidean distance between the reference image patch B^r and each of other image patches in a neighbor with the size of $W \times W$, then select the $m-1$ smallest Euclidean distance with the reference image patch B^r as the most similar ones to the reference patch B_r, thus obtain a similar patch group which has altogether m image patches. The Euclidean distance is calculated as the following:

$$D_B^{ri} = \|B_r - B_i\|_2^2, (i = 1, \cdots, W \times W) \tag{4}$$

Each image patch with the size of $\sqrt{n} \times \sqrt{n}$ is stretched into a column vector $M_{b,i} \in \mathbb{R}^n$ ($i = 1, \ldots, m$). Then all $M_{b,i}$ are stacked into a new matrix $M_b = [M_{b,1}, \ldots, M_{b,m}] \in \mathbb{R}^{n\times m}$.

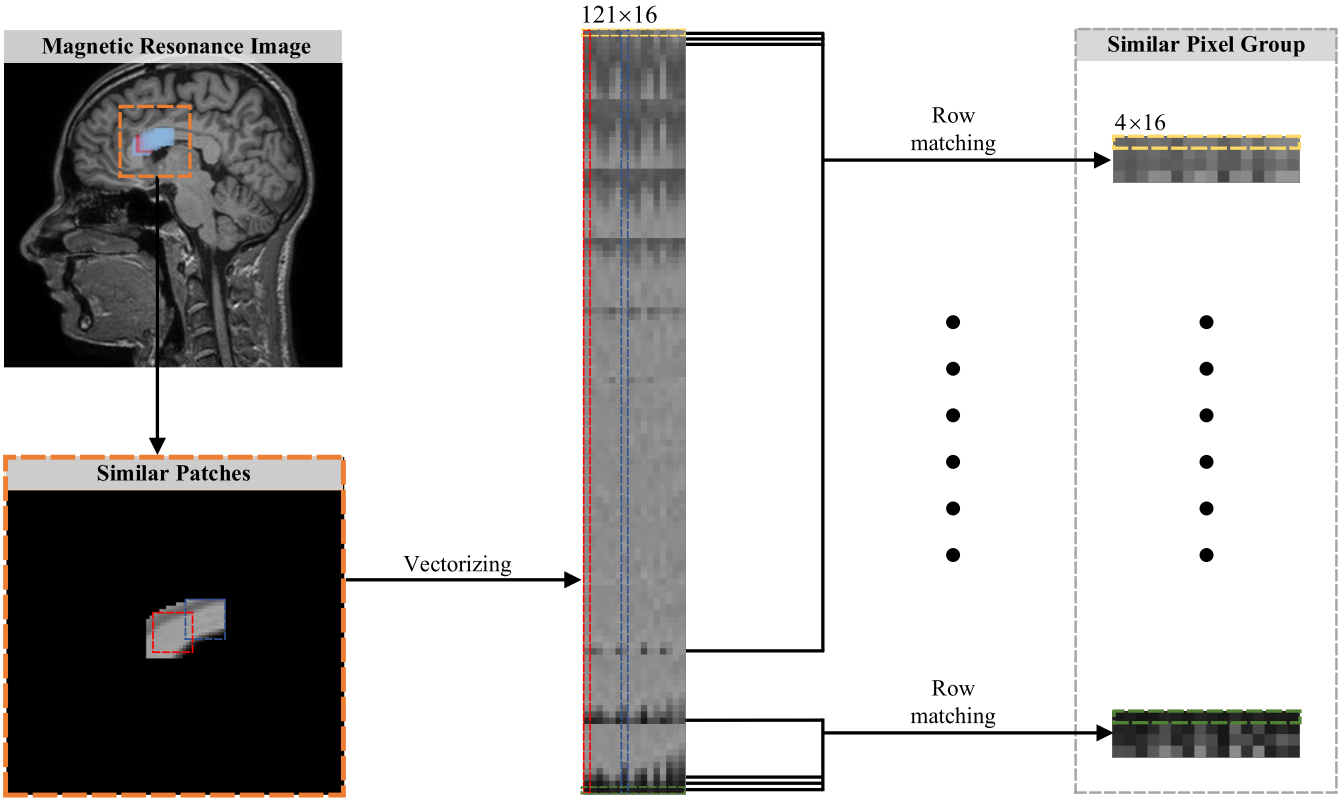

FIGURE 2. Illustration of the similar pixel grouping procedure.

b: ROW-MATCHING

In order to effectively explore the pixel-level self-similarity in the image, we also perform row-matching in all of the M_b (see Figure 2). We use the reference row M_b^r (the r-th in M_b) $\in (\mathbb{R}^m)^T$ to calculate the Euclidean distance between each of other rows, the smallest distance value means the most similar row, we can obtain similar $q-1$ rows by this method, then put together M_b^r with the most similar $q-1$ rows to construct the similar pixel group $M_p \in \mathbb{R}^{q\times m}$. The Euclidean distance between the reference row and each of other rows is also calculated as the following:

$$d_B^{rj} = \left\| M_b^r - M_b^j \right\|_2^2, (j = 1, \cdots, n) \tag{5}$$

c: BI-HARD THRESHOLDING-BASED BASIC REFINEMENT

As shown the upper part in Figure 3, we implement a separable Haar transform on each similar pixel group $M_p \in \mathbb{R}^{q\times m}$ [37], [38]. The 2-D transform on the non-local similar pixel group M_p obtains the transformed coefficient matrix $C_p \in \mathbb{R}^{q\times m}$ as the following:

$$C_p = H_l M_p H_r \tag{6}$$

where the two 2-D Haar transform matrices $H_l \in \mathbb{R}^{q\times q}$ and $H_r \in \mathbb{R}^{m\times m}$ are both orthogonal.

The fully similarity on each similar pixel group ensures the sparsity of the transformed spectrum C_p, so we can use a hard-thresholding strategy to effectively remove the artifacts. The proposed undersampled MRI image refinement reconstruction is like image denoising, however, the noise level is unknown in advance, so we use a set of noise level which take values according to the decreasing logarithmic spacing vector σ_s in each step iteration:

$$\hat{C}_p = C_p \odot \mathcal{X}_h \tag{7}$$

where $\odot$ means element-wise production, $\mathcal{X}_h \in \mathbb{Z}^{q\times m}$ is an indicator function which is used to the coefficient hard-thresholding. The values of $\mathcal{X}_h$ are as follows:

$$\mathcal{X}_h(i,j) = \begin{cases} 1, & \left|C_p(i,j)\right| \geq \tau\sigma_s; \\ 0, & \left|C_p(i,j)\right| < \tau\sigma_s. \\ (i = 1, \cdots, q;\ j = 1, \cdots, m.) \end{cases} \tag{8}$$

where τ is the hard-thresholding parameter. Additionally, the fully similarity also ensures all the coefficients excepting for the 1-st row and the 1-st column ones are all from the artifacts. To more effectively remove the artifacts, we utilize a structural hard-thresholding strategy, i.e., completely set 0 to all the coefficients in the high frequency regions of $\hat{C}_p$:

$$\tilde{C}_p = \hat{C}_p \odot \mathcal{X}_s \tag{9}$$

where $\mathcal{X}_s \in \mathbb{Z}^{q\times m}$ is also an indicator function which is used to the structural hard-thresholding. The values of $\mathcal{X}_s$ are

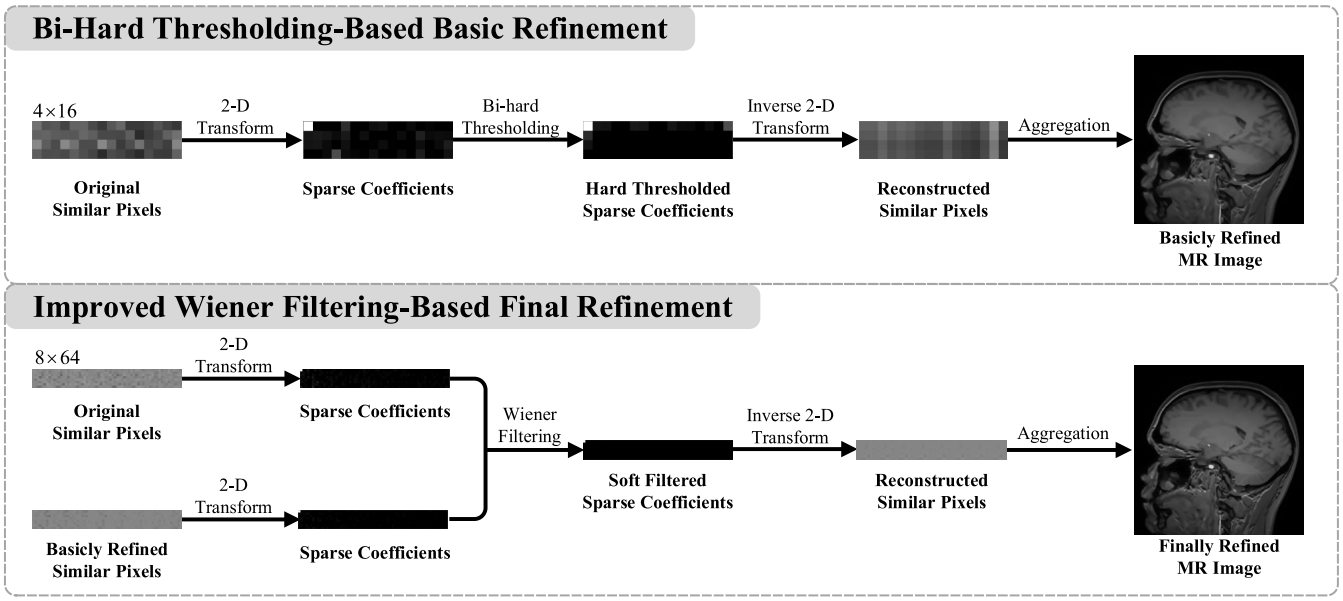

FIGURE 3. Illustration of the pixel-level non-local method based MRI refinement.

as follows:

$$\mathcal{X}_s(i,j) = \begin{cases} 0, & i = 2, \cdots, q, \quad j = 2, \ldots, m; \\ 1, & others. \end{cases} \tag{10}$$

The inverse 2-D separable Haar transforms on $\tilde{C}_p$ is used to obtain the basicly estimated similar pixel group $\tilde{M}_p$:

$$\tilde{M}_p = H_l^T \tilde{C}_p H_r^T \tag{11}$$

where $H_l^T \in \mathbb{R}^{q\times q}$ and $H_r^T \in \mathbb{R}^{m\times m}$ are inverse matrices of 2-D Haar transform matrices H_l and H_r due to the orthogonality, respectively. Finally, we aggregate all the basicly estimated pixel groups $\{\tilde{M}_p\}_{b=1}^N$ to obtain the basicly refined MRI image reconstruction result $\tilde{I}_k$.

d: IMPROVED WIENER FILTERING-BASED FINAL REFINEMENT

In the first stage, the reconstructed MRI image $\tilde{I}_k$ is only a basic refinement of the preliminary reconstructed MRI image. In this stage (see the lower part of Figure 3), the basic refinement result is used as a reference image to the Wiener filtering to further refine reconstruction results. To better remove artifacts and preserve more details, we employ an improved Wiener filtering strategy by combining the basicly refined image $\tilde{I}_k$ with the previous iteration result image $\overline{I}_{k-1}$ to better restore image detail signals:

$$\tilde{I}_{kc} = \alpha \tilde{I}_k + (1-\alpha)\overline{I}_{k-1} \tag{12}$$

where $\overline{I}_{k-1}$ is the reconstructed MRI image of the previous iteration. $\tilde{I}_{kc}$ is the combining of $\overline{I}_{k-1}$ and $\tilde{I}_k$, which is used as the reference image in the actual implementation of the Wiener filtering. We still use the predefined noise level σ_s to perform an improved Wiener filtering process on the two coefficients matrices $\tilde{C}_p^w$ and $\overline{C}_p^w$, which are obtained by the 2-D separable Haar transform on similar pixel groups of basicly refined result image $\tilde{I}_k$ and the previous iteration result image $\overline{I}_{k-1}$, respectively. We implement the improved Wiener filtering:

$$\tilde{\tilde{C}}_p^w(i,j) = \frac{\left(\alpha \tilde{C}_p^w(i,j) + (1-\alpha)\overline{C}_p^w(i,j)\right)^2}{\left(\alpha \tilde{C}_p^w(i,j) + (1-\alpha)\overline{C}_p^w(i,j)\right)^2 + (\sigma_s)^2} \overline{C}_p^w(i,j) \tag{13}$$

where i, j means the i-th row and the j-th column element of the corresponding matrices. It is to be noted that the Eq. 13 has a little bit difference from the classic Wiener filtering, we add a part of the previous step coefficients to better preserve the real signals. Considering that there are some real signals in $\tilde{C}_p^w$ have been removed by the basic refinement stage, we use $\alpha\tilde{C}_p^w + (1-\alpha)\overline{C}_p^w$ to take place of $\tilde{C}_p^w$ of the traditional Wiener filtering method to avoid excessive detail loss. The inverse 2-D separable Haar transform on $\tilde{\tilde{C}}_p^w$ is used to obtain the final reconstructed pixel group $\overline{M}_{(p,k)}$ in the k-th iteration. We aggregate all the reconstructed pixel groups $\{\overline{M}_{(p,k)}\}_{p=1}^n$ to obtain the k-th iteration reconstructed MRI image $\overline{I}_k$.

3) ALGORITHM PSEUDOCODE

The proposed pixel-level non-local method based compressed sensing magnetic image reconstruction model includes two parts: pixel-level non-local refinement (PNR) and compressed sensing (PNCS). The detailed two algorithm pseudocodes is shown in Algorithm 1 and 2, respectively.

Algorithm 1 PNR: Pixel-Level Non-Local Refinement

Data: The k-th pixel-level non-local refinement input image $\bar{I}_k \in \mathbb{R}^{\sqrt{N}\times\sqrt{N}}$

Result: The k-th refined image $\tilde{\bar{I}}_k \in \mathbb{R}^{\sqrt{N}\times\sqrt{N}}$

Function PNR $(\bar{I}_k, \sigma)$ **:**

(1) Patch matching (Eq. 4): Acquiring similar patch group $M_b \in \mathbb{R}^{n\times m}$ from $\bar{I}_k$;

(2) Row matching (Eq. 5): Acquiring similar pixel group $M_p \in \mathbb{R}^{q\times m}$;

(3) 2-D transform and Bi-Hard thresholding (Eq. 6∼Eq. 11): Acquiring basicly refined image $\tilde{\bar{I}}_k$;

(4) Improved Wiener-filtering (Eq. 12∼Eq. 13): Acquiring finally refined image $\tilde{\tilde{\bar{I}}}_k$ in the k-th iteration;

return $\tilde{\tilde{\bar{I}}}_k$.

Algorithm 2 PNCS: Pixel-Level Non-Local Compressed Sensing

Data: The reconstructed zero-filled MRI image $I_0 \in \mathbb{R}^{\sqrt{N}\times\sqrt{N}}$

Result: The reconstructed MRI image $\bar{I} \in \mathbb{R}^{\sqrt{N}\times\sqrt{N}}$

Function PNCS $(I_0, \sigma, M, stepnum, iternum)$ **:**

$\bar{I}_1 = I_0$;

for $s = 1 \rightarrow stepnum$ **do**

  for $l = 1 \rightarrow iternum_s$ **do**

    (1) $\bar{I}_{s,l} = PNR(\bar{I}_s, \sigma_s)$, (§II-B2);

    (2) $FFT(\bar{I}_{s,l}) = FFT(I_0) + FFT(\bar{I}_{s,l}) \odot M$, (Eq. 3);

    (3) $\bar{I}_{s,l} = IFFT(FFT(\bar{I}_{s,l}))$, (§II-B1);

    (4) $\bar{I}_s = \bar{I}_{s,l}$;

$\bar{I} = \bar{I}_s$;

return $\bar{I}$.

4) COMPLEXITY ANALYSIS

The proposed PNCS model includes two parts: (1) In §II-B1, the complexity of FFT and IFFT reconstruction is $O(hwlog(hw))$. (2) For §II-B2, in each iteration, the complexity of stage (1) and stage (2) is $O(NW^2n)$, the complexity of stage (3) and (4) is $O(Nnqm)$. Since we have $W^2 > step^2$ and $n > log(hw)$, the complexity of our PNCS is $O(KNW^2n)$, where K means the total number of iterations.

III. RESULTS

The actual implementation of the proposed PNCS model will be introduced in detail, including the data collection, parameters, and evaluation metrics in §III-A. We then present the comparison with the state-of-the-art CS-MRI methods on different MRI image datasets in §III-B1 both on objective and subjective evaluation.

A. IMPLEMENTATION DETAILS

1) DATA COLLECTION

a: DATASETS

We conduct comparison experiments on simulated undersampled MRI image reconstruction with other state-of-the-art methods on the fastMRI [41][1] single-coil knee dataset and multi-coil brain dataset, respectively. Among them, the single-coil knee dataset consists of two parts, coronal proton density with (PDFS) or without (PD) fat saturation, while the multi-coil brain dataset consists of four parts, AXT1, AXT2, AXT1POST, and AXFLAIR. For each part of the single-coil knee and the multi-coil brain dataset mentioned above, 6 volumes were randomly selected for testing. Note that, in order to avoid the influence of less informative slices on the accuracy of the overall results, we removed the first 5 slices and the last 5 slices of each volume in the single-coil knee dataset, and only removed the last slice in the multi-coil brain dataset.

b: MASKS

We test undersampled data on Cartesian sampling method. Each mask simulates 25% and 12.5% of the original k-space data retained, representing 4× and 8× acceleration, respectively. According to the settings in fastMRI [41], the mask retains full sampling in the middle part and random sampling in the rest. For the 4× accelerated reconstruction task, the central fully sampled area of the mask used accounts for 8% of all k-space lines, while in the 8× accelerated reconstruction task, the central fully sampled area accounts for 4%.

main

2) PARAMETERS

The pixel-level non-local refinement stage includes 6 main parameters in basic refinement and final refinement, respectively. Where patch size is $\sqrt{n}$, window size for searching similar patches is W, number of similar patches is m, number of similar pixel row is q, regularization parameter is α, hard-thresholding parameter is τ, and reference patch sliding step size is N_{step}. The concrete parameter values of steps 1) - 3) in §II-B2 are as follows, $\sqrt{n} = 13$, $W = 23$, $m = 16$, $q = 4$, $\tau = 6.0$, and $N_{step} = 12$. In the 4) step in §II-B2, we set $\sqrt{n} = 21$, $W = 13$, $m = 64$, $q = 8$, $\alpha = 0.5$, and $N_{step} = 21$. The maximum noise standard deviation $\sigma_1 = 80$ in the first step iteration, but the minimum noise standard deviation is just $\sigma_K = 1.33$, others σ_k take the values respectively according to the decreasing logarithmic spacing vector. The number of inner cycles of each iteration according to the minimum value $s_{min} = 5$ and the maximum value $s_{max} = 21$ takes the increasing logarithmic spacing vector values. Where the number of maximum iteration $K = 100$.

3) METRICS

To validate the performance of different methods, we calculate the Peak Signal-to-Noise Ratio (PSNR) and Structural

[1] https://fastmri.med.nyu.edu/

TABLE 1. Quantitative results (PSNR and SSIM) of a comparative study using 4× and 8× accelerations on the fastMRI single-coil knee dataset. The best and second best results are highlighted in red and blue, respectively.

Acceleration	PD/PDFS	Metric	ZF	TV [7]	BM3D-AMP [39]	PANO [24]	U-Net [34]	MC-DDPM [40]	PNCS (ours)
4×	PD	PSNR	28.55	36.50	34.07	38.31	33.33	38.23	41.22
		SSIM	0.8735	0.9531	0.9271	0.9643	0.9448	0.9287	0.9790
	PDFS	PSNR	30.05	37.38	35.17	38.81	32.47	36.36	39.98
		SSIM	0.8594	0.9247	0.8937	0.9386	0.8541	0.8432	0.9480
8×	PD	PSNR	24.02	30.64	28.07	31.50	32.57	34.58	34.90
		SSIM	0.7593	0.8719	0.8197	0.8844	0.9259	0.8887	0.9385
	PDFS	PSNR	26.81	33.61	29.62	34.56	32.01	34.23	36.34
		SSIM	0.7796	0.8169	0.8026	0.8839	0.8407	0.8128	0.9117

TABLE 2. Quantitative results (PSNR and SSIM) of a comparative study using 4× and 8× accelerations on the fastMRI multi-coil brain dataset. The best and second best results are highlighted in red and blue, respectively.

Acceleration	Sequence	Metric	ZF	TV [7]	BM3D-AMP [39]	PANO [24]	U-Net [34]	PNCS (ours)
4×	AXT1	PSNR	30.51	35.58	34.52	39.61	38.49	43.31
		SSIM	0.8770	0.9495	0.9303	0.9655	0.9687	0.9804
	AXT2	PSNR	29.40	33.66	33.87	36.83	37.30	41.22
		SSIM	0.8627	0.9372	0.9326	0.9525	0.9670	0.9756
	AXT1POST	PSNR	31.00	37.69	36.65	41.60	39.24	44.88
		SSIM	0.8878	0.9650	0.9492	0.9763	0.9752	0.9862
	AXFLAIR	PSNR	31.72	35.24	31.40	37.44	38.70	40.94
		SSIM	0.8873	0.9377	0.8976	0.9503	0.9660	0.9705
8×	AXT1	PSNR	27.07	29.76	30.20	32.52	33.41	37.84
		SSIM	0.8061	0.8787	0.8661	0.9002	0.9269	0.9584
	AXT2	PSNR	26.41	28.32	28.98	29.78	32.97	34.46
		SSIM	0.7879	0.8555	0.8577	0.8655	0.9205	0.9447
	AXT1POST	PSNR	26.95	30.78	32.81	33.75	34.43	39.64
		SSIM	0.8084	0.9009	0.9037	0.9210	0.9457	0.9699
	AXFLAIR	PSNR	28.61	30.59	27.57	31.43	35.41	35.38
		SSIM	0.8257	0.8781	0.8165	0.8839	0.9289	0.9418

Similarity Index (SSIM) [42] for all reconstructed images. We take the reconstructed fully sampled MRI images as the ground-truth. Note that, considering that the inter-image calculation may ignore the overall image structure. We follow the fastMRI [41] recommendation to calculate PSNR and SSIM in terms of volumes. The PSNR value is calculated as the following:

$$PSNR(\hat{v}, v) = 10 \log_{10} \frac{\max(v)^2}{MSE(\hat{v}, v)} \tag{14}$$

where $\hat{v}$ is the reconstructed volume, v is the ground truth volume, $\max(v)$ is the largest entry in the ground truth volume v, $MSE(\hat{v}, v)$ is the mean square error between $\hat{v}$ and v defined as $\frac{1}{n}\|\hat{v}-v\|_2^2$, and n is the number of entries in the ground truth volume v. The higher value of PSNR indicates the better reconstruction.

B. COMPARISON WITH STATE-OF-THE-ART METHODS

1) RESULTS ON SINGLE-COIL KNEE DATA

a: COMPARISON METHODS

We compared our PNCS model with conventional CS-MRI methods, including TV [7], and the state-of-the-art methods, including BM3D-AMP [39], PANO [24], U-Net [34], and MC-DDPM [40]. Here, except for the random noise filling reconstruction used in the BM3D-AMP [39] to initialize, the other methods and our PNCS model are initialized with the baseline zero-filling (ZF) reconstruction of the undersampled k-space data.

b: RESULTS

Table 1summarizes the PSNR and SSIM scores of the reconstructions obtained by conventional CS-MRI and some representative state-of-the-art methods on the fastMRI single-coil knee datasets. The 4× accelerated reconstruction results show that the simple zero-padded images do not achieve satisfactory PNSR or SSIM scores for PD or PDFS images. TV [7] shows good performance in both PD and PDFS reconstruction. The BM3D-AMP [39] achieves significant improvement compared to the baseline ZF, but it can only achieve similar performance to TV. The patch-based non-local operator proposed by PANO [24] significantly improves the performance of undersampled MRI reconstruction, however, it is still slightly weaker than our PNCS model. U-Net [34] does not obtain very satisfactory results in the 4× task. Although MC-DDPM [40] achieves a high PSNR score, the SSIM score is not very high in comparison. In contrast, our PNCS model achieves the highest scores in PD and PDFS image reconstruction tasks. The 8× accelerated reconstruction results show that the PSNR and SSIM scores of all methods have decreased significantly due to the further reduction of the k-space signal. It is worth noting that the performance of the DNN-based methods (U-Net [34] and

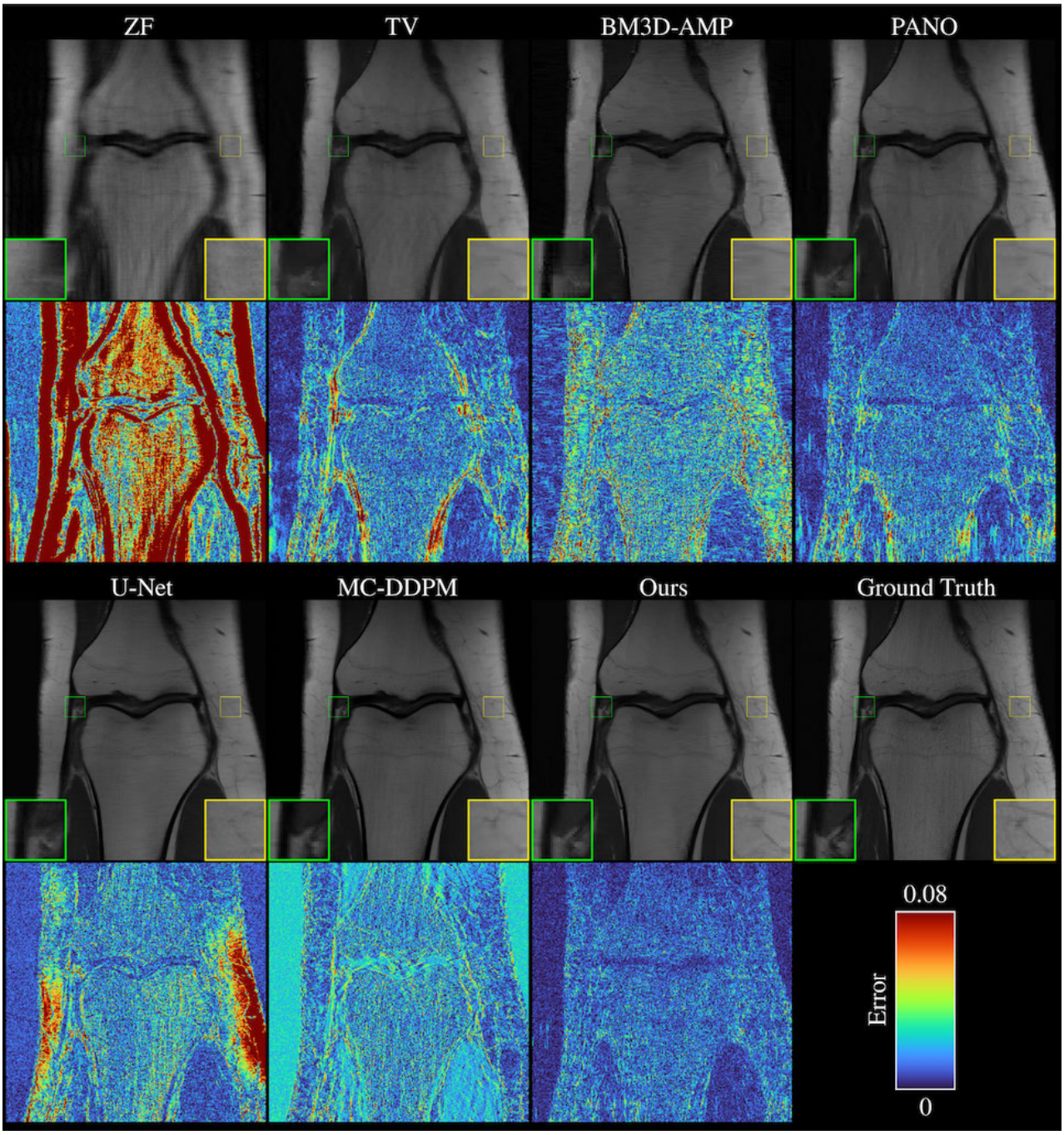

FIGURE 4. Reconstructions of PD images from the fastMRI single-coil knee dataset at 4× acceleration. The 1-st and 3-rd rows show the reconstruction results of different methods, respectively. The 2-nd and 4-th rows show the corresponding error maps.

MC-DDPM [40]) in the 8× accelerated reconstruction task is significantly improved, however, the overall performance of our PNCS method is still competitive to these DNN-based methods.

The visually qualitative results of 4× accelerated reconstructions of PD and PDFS images are shown in Figure 4 and Figure 5, respectively. Due to space limitations, the 8× accelerated reconstruction results for PD and PDFS images will be presented in the supplementary material. One can see that the reconstructions obtained by the baseline ZF contain many artifacts, covering most of the details of the MRI image. TV [7] can eliminate some artifacts in the reconstructions, however, the reconstructions tend to be over-smoothed. BM3D-AMP can maintain good structural consistency but unsatisfactory performance on artifact reduction. The reconstructions of PANO [24] appear to have fewer artifacts as a whole, however, the edge and detail information is not well preserved. U-Net [34] achieves decent results, however, as can be seen from the corresponding error maps, its performance is still not better than our PNCS model.

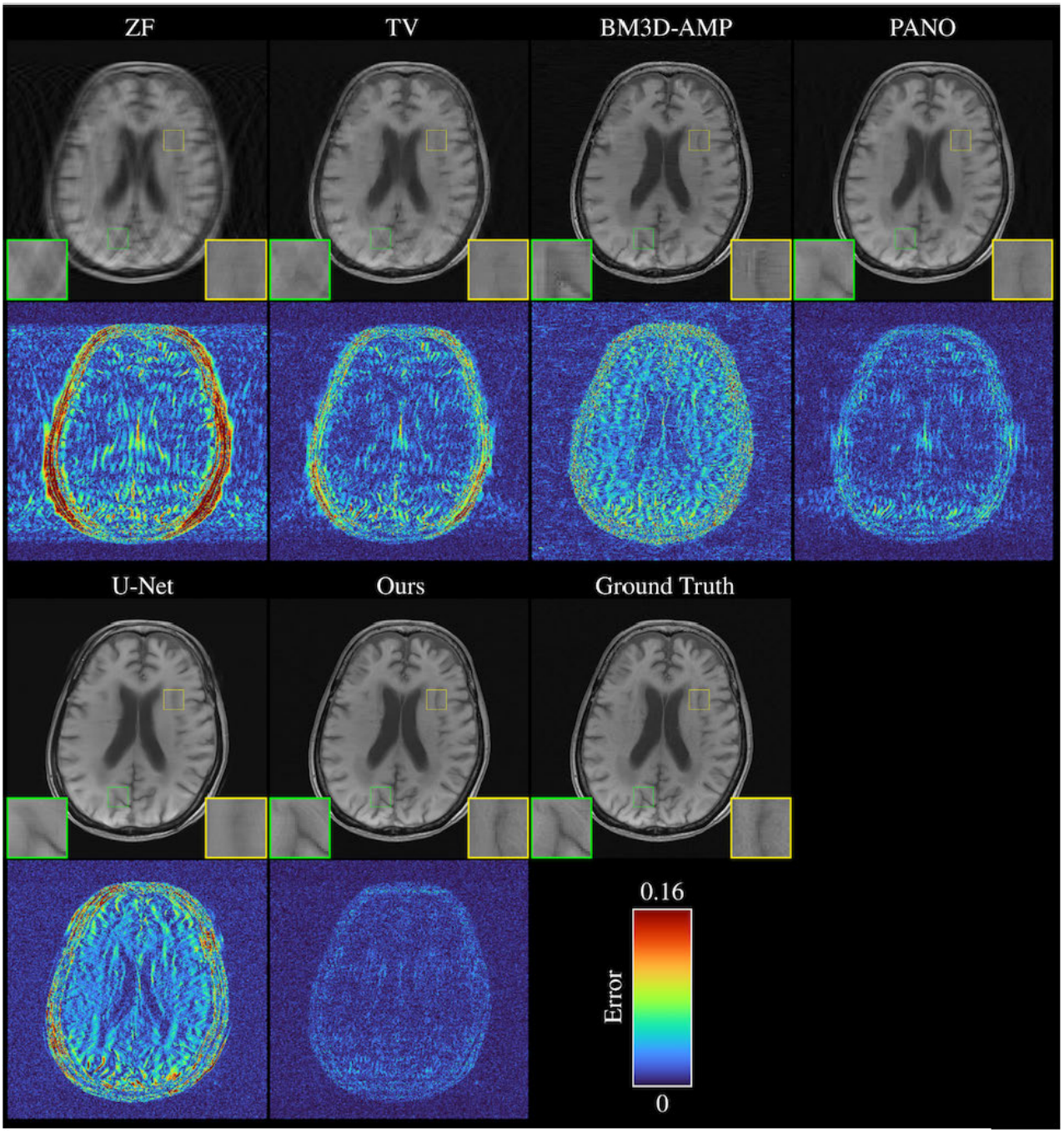

FIGURE 5. Reconstructions of PDFS images from the fastMRI single-coil knee dataset at 4× acceleration. The 1-st and 3-rd rows show the reconstruction results of different methods, respectively. The 2-nd and 4-th rows show the corresponding error maps.

The results obtained by MC-DDPM [40] are acceptable in subjective visual quality, however, the corresponding error maps show a significant deviation from the ground-truth. In contrast, our PNCS model shows the best results on both subjective visual quality and corresponding error maps.

2) RESULTS ON MULTI-COIL BRAIN DATA

a: COMPARISON METHODS

In this study, we cancel the comparison with MC-DDPM because it lacks a pre-trained model for the multi-coil brain dataset, and we cannot retrain the model due to computational constraints. The other methods compared are the same as those described in §III-B1.

b: RESULTS

In the results of the 4× accelerated reconstruction, it can be seen that the baseline ZF still exhibits the weakest performance. The overall performance of the TV [7] is acceptable, but the reconstruction results of the AXT2 images achieve slightly lower scores. The reconstruction performance of

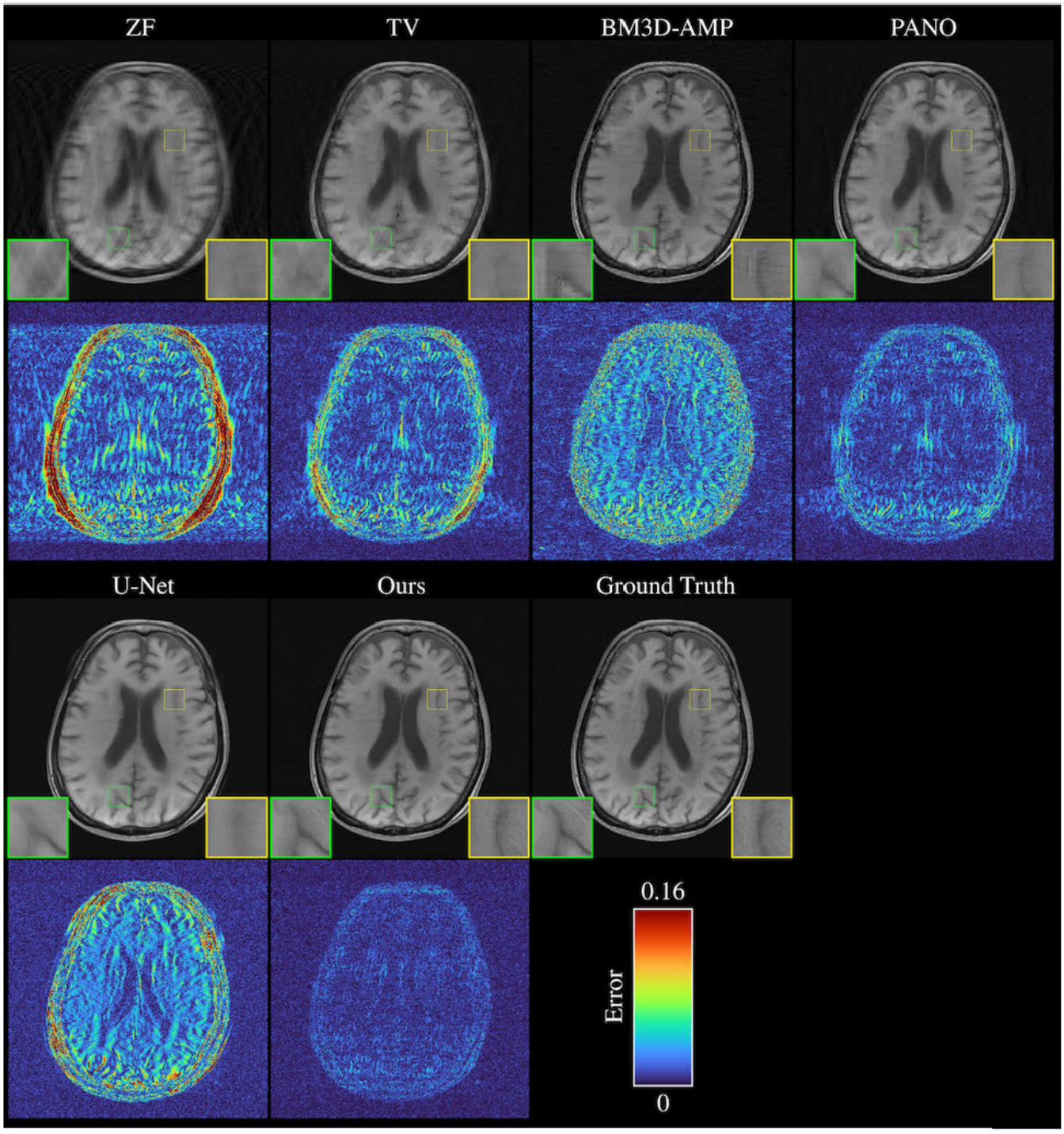

FIGURE 6. Reconstructions of AXT1 images from the fastMRI multi-coil brain dataset at 4× acceleration. The 1-st and 3-rd rows show the reconstruction results of different methods, respectively. The 2-nd and 4-th rows show the corresponding error maps.

BM3D-AMP [39] for AXT2 images is slightly more robust than that of TV [7], however, the reconstruction performance of other kinds of sequence images is still not better than that of TV, which is especially obvious in the reconstruction of AXFLAIR images. PANO [24] achieves satisfactory scores overall, but the reconstruction performance for AXT2 and AXFLAIR images is still not better than U-Net. The overall performance of U-Net [34] is better than that of PANO [24], but it exhibits some disadvantages in reconstructing AXT1POST images. In contrast, our PNCS method achieves the highest PSNR and SSIM scores in all four sequence image reconstruction tasks, shows relatively better performance then each of the comparison methods. The overall performance ranking of the different methods of the 8× accelerated reconstruction is similar to the results of 4× accelerated reconstruction. The difference is that the

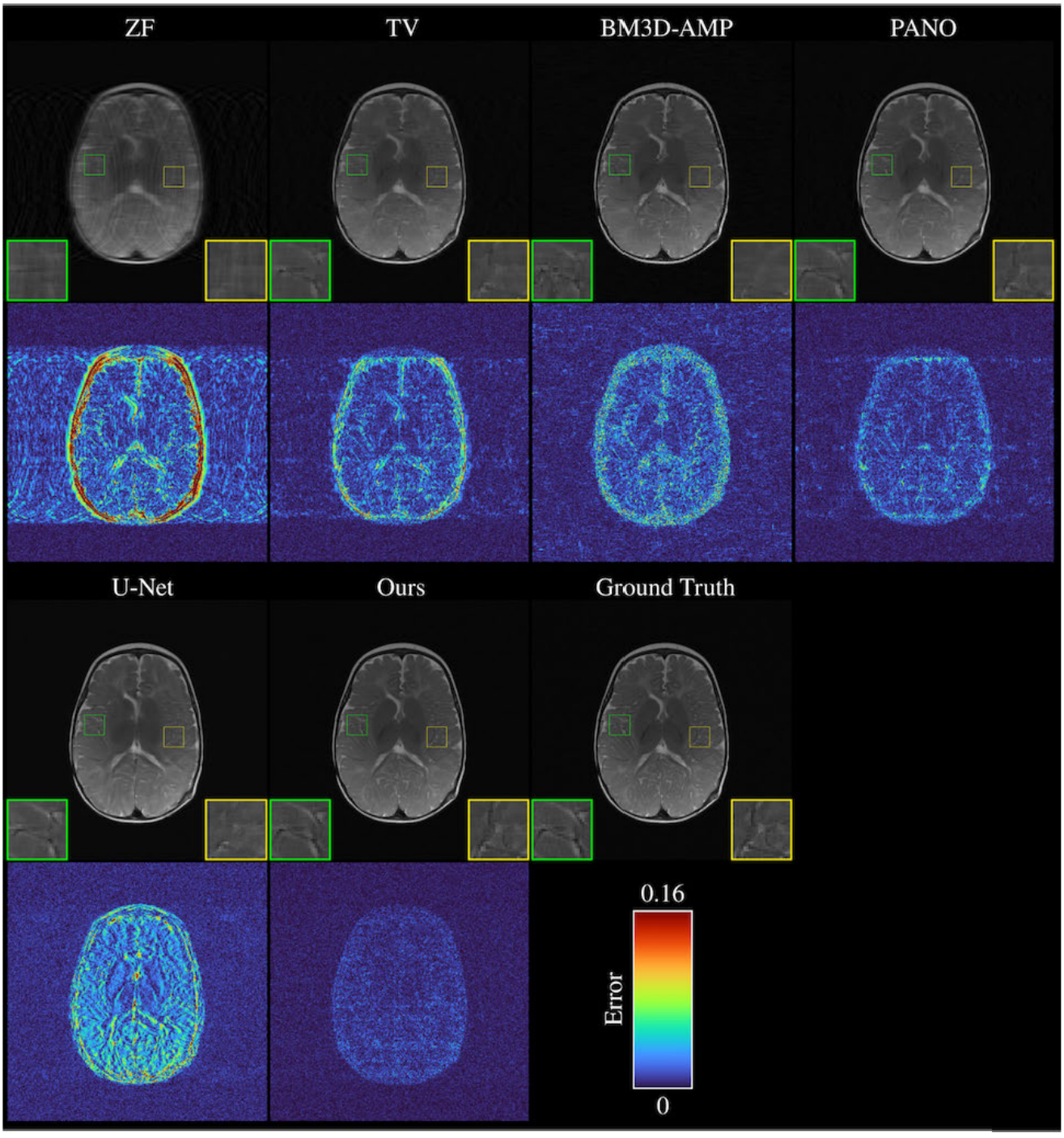

FIGURE 7. Reconstructions of AXT2 images from the fastMRI multi-coil brain dataset at 4× acceleration. The 1-st and 3-rd rows show the reconstruction results of different methods, respectively. The 2-nd and 4-th rows show the corresponding error maps.

overall performance of PANO [24] has a significant gap with U-Net [34]. U-Net [34] achieves the highest PSNR score in the reconstruction task of AXFLAIR images, however, in general, our PNCS method still shows the most robust performance.

The qualitative results of the visual quality of the AXT1, AXT2 image reconstruction results are shown in Figure 6, Figure 7, respectively. Due to space limitations, the 4× accelerated reconstruction results for AXT1 and AXT2 images and the 8× accelerated reconstruction results for AXT1, AXT2, AXT1POST, and AXFLAIR images are all presented in the supplementary material. It can be seen that ZF not only fails to preserve the image details but also the artifacts are not effectively removed in the reconstructed images. Its corresponding error maps produce very noticeable deviations at the edges of the image. Although the reconstruction results of TV [7] can remove some artifacts, there is still much room for improvement in preserving image details. The reconstruction

results of BM3D-AMP [39] are slightly better than TV, but the image details are not well preserved either. PANO [24] achieves good results in artifacts removal and details preservation, however, its results are still not better than our PNCS model. U-Net [34] removes artifacts well, however, its results still lack some details compared to the results obtained by our PNCS method, which can be seen from the corresponding error maps. In contrast, our PNCS effectively removes artifacts introduced by undersampling reconstruction and outperforms other methods in detail preservation.

IV. DISCUSSION

In the proposed pixel-level non-local method based compressed sensing undersampled MRI image reconstruction model, the pixel-level non-local method is used to remove the artifacts gradually in each iteration. The main goal of the original non-local idea is to be used for image denoising [43], [44], [45]. PANO [24] proposed a patch-level non-local method based undersampled CS-MRI reconstruction, however, the artifacts introduced by the undersampling reconstruction usually tends to be mistaken for the real signals, so effectively removing artifacts inevitably over-smoothing image details.

In recent years, many DNN-based methods were developed to deal with the undersampled MRI image reconstruction problem. Although these methods can achieve competitively reconstruction results, they have a common problem that each kind of undersampling mode should be trained respectively, this limits the generalization of these methods.

Although, the pixel-level non-local self-similarity has been proposed to deal with the image denoising problem initially [36], especially for real-world image denoising. As described in this method [36], the noise in a real-world image is generally not Gaussian distribution ones, the noise in real- world images appear plaques or line-like, the procedure of block-matching and row-matching operations, especially the row-matching can effectively change this kind of noise to pseudo-Gaussian noise. Inspired by this opinion, the artifacts in undersampled reconstruction images also looks like the above mentioned noise, so we propose to apply this idea to deal with the undersampled MRI image reconstruction problem.

We use fewer and smaller parameters in the proposed method than the pixel-level denoising method [36]. In each iteration refinement step, we remove the iteration steps and just implement one step hard-thresholding and one step Wiener filtering in each iteration refinement step. The utilization of the original sampled signals also plays an important role, if this part of the signal is not reused in each iteration, the reconstructed image will be gradually smoothed, and the main details in the image will be lost.

Despite achieving desirable performance, our study has several limitations. Compared with the DNN-based methods optimized by GPU acceleration, the proposed method needs a much longer running time. There is a lack of optimal iteration times for different images and undersampling modes. We have tried to solve this problem with ℓ_0-norm or ℓ_1-norm of the reconstructed MRI image, but they are not very successful. It is not practical to use PSNR or SSIM values to determine the number of iterations. Fortunately, through a large number of experiments, we found that almost all images and sampling modes can achieve sub-optimal results using the proposed algorithm for 30 iterations. All our experimental results are based on this number of iterations. In the future, we will further research these problems to reduce the algorithm complexity and find an optimal iteration termination rule.

V. CONCLUSION

In this study, we propose an iterative refinement reconstruction model based on a pixel-level non-local method for CS-MRI reconstruction. This method can better explore the non-local self-similarity of images than the patch-level non-local method, and thus better represent the sparsity of MRI images. Enhanced sparsity representation can help remove artifacts in undersampled MRI image reconstruction. The main contribution of this method is that, compared with similar patch grouping methods, similar pixel grouping can better separate artifacts from real signals. In fact, this method can change artifacts into pseudo-random noise. Simple Haar transform can further effectively separate noise from the real signal, so this method can better achieve undersampled MRI image reconstruction than traditional patch-level non-local methods.

REFERENCES

[1] A. Oppelt, R. Graumann, H. Barfuss, H. Fischer, W. Hartl, and W. Schajor, "FISP—A new fast MRI sequence," *Electromedica*, vol. 54, no. 1, pp. 15–18, 1986.
[2] H. K. Hussain, F. J. Londy, I. R. Francis, H. V. Nghiem, W. J. Weadock, A. Gebremariam, and T. L. Chenevert, "Hepatic arterial phase MR imaging with automated bolus-detection three-dimensional fast gradient-recalled-echo sequence: Comparison with test-bolus method," *Radiology*, vol. 226, no. 2, pp. 558–566, Feb. 2003.
[3] R. N. Low, I. R. Francis, J. S. Sigeti, and T. K. Foo, "Abdominal MR imaging: Comparison of T_2-weighted fast and conventional spin-echo, and contrast-enhanced fast multiplanar spoiled gradient-recalled imaging," *Radiology*, vol. 186, no. 3, pp. 803–811, Mar. 1993.
[4] S.-G. Kim, K. Hendrich, X. Hu, H. Merkle, and K. Uğurbil, "Potential pitfalls of functional MRI using conventional gradient-recalled echo techniques," *NMR Biomed.*, vol. 7, nos. 1–2, pp. 69–74, Mar. 1994.
[5] D. K. Sodickson and W. J. Manning, "Simultaneous acquisition of spatial harmonics (SMASH): Fast imaging with radiofrequency coil arrays," *Magn. Reson. Med.*, vol. 38, no. 4, pp. 591–603, 1997.
[6] M. A. Griswold, P. M. Jakob, R. M. Heidemann, M. Nittka, V. Jellus, J. Wang, B. Kiefer, and A. Haase, "Generalized autocalibrating partially parallel acquisitions (GRAPPA)," *Magn. Reson. Med.*, vol. 47, no. 6, pp. 1202–1210, 2002.
[7] M. Lustig, D. Donoho, and J. M. Pauly, "Sparse MRI: The application of compressed sensing for rapid MR imaging," *Magn. Reson. Med.*, vol. 58, no. 6, pp. 1182–1195, Oct. 2007.
[8] K. T. Block, M. Uecker, and J. Frahm, "Undersampled radial MRI with multiple coils. Iterative image reconstruction using a total variation constraint," *Magn. Reson. Med.*, vol. 57, pp. 1086–1098, Jun. 2007.
[9] J. Yang, Y. Zhang, and W. Yin, "A fast alternating direction method for TVL1-L2 signal reconstruction from partial Fourier data," *IEEE J. Sel. Topics Signal Process.*, vol. 4, no. 2, pp. 288–297, Apr. 2010.
[10] F. Knoll, K. Bredies, T. Pock, and R. Stollberger, "Second order total generalized variation (TGV) for MRI," *Magn. Reson. Med.*, vol. 65, no. 2, pp. 480–491, 2011.

[11] X. Qu, Di Guo, B. Ning, Y. Hou, Y. Lin, S. Cai, and Z. Chen, "Undersampled MRI reconstruction with patch-based directional wavelets," *Magn. Reson. Imag.*, vol. 30, no. 7, pp. 964–977, Sep. 2012.

[12] Z. Zhu, K. Wahid, P. Babyn, and R. Yang, "Compressed sensing-based MRI reconstruction using complex double-density dual-tree DWT," *Int. J. Biomed. Imag.*, vol. 2013, pp. 1–12, Jan. 2013.

[13] Z. Lai, X. Qu, Y. Liu, Di Guo, J. Ye, Z. Zhan, and Z. Che, "Image reconstruction of compressed sensing MRI using graph-based redundant wavelet transform," *Med. Image Anal.*, vol. 27, pp. 93–104, Jan. 2016.

[14] M. Hong, Y. Yu, H. Wang, F. Liu, and S. Crozier, "Compressed sensing MRI with singular value decomposition-based sparsity basis," *Phys. Med. Biol.*, vol. 56, no. 19, pp. 6311–6325, Oct. 2011.

[15] S. G. Lingala and M. Jacob, "Blind compressive sensing dynamic MRI," *IEEE Trans. Med. Imag.*, vol. 32, no. 6, pp. 1132–1145, Jun. 2013.

[16] Y. Wang and L. Ying, "Undersampled dynamic magnetic resonance imaging using kernel principal component analysis," in *Proc. 36th Annu. Int. Conf. IEEE Eng. Med. Biol. Soc.*, Aug. 2014, pp. 1533–1536.

[17] S. Ravishankar and Y. Bresler, "MR image reconstruction from highly undersampled k-space data by dictionary learning," *IEEE Trans. Med. Imag.*, vol. 30, no. 5, pp. 1028–1041, May 2011.

[18] J. Caballero, A. N. Price, D. Rueckert, and J. V. Hajnal, "Dictionary learning and time sparsity for dynamic MR data reconstruction," *IEEE Trans. Med. Imag.*, vol. 33, no. 4, pp. 979–994, Apr. 2014.

[19] Z. Zhan, J.-F. Cai, D. Guo, Y. Liu, Z. Chen, and X. Qu, "Fast multiclass dictionaries learning with geometrical directions in MRI reconstruction," *IEEE Trans. Biomed. Eng.*, vol. 63, no. 9, pp. 1850–1861, Sep. 2016.

[20] W. Yin, S. Osher, D. Goldfarb, and J. Darbon, "Bregman iterative algorithms for ℓ_1-minimization with applications to compressed sensing," *SIAM J. Imag. Sci.*, vol. 1, no. 1, pp. 143–168, 2008.

[21] R. Chartrand, "Fast algorithms for nonconvex compressive sensing: MRI reconstruction from very few data," in *Proc. IEEE Int. Symp. Biomed. Imag., Nano Macro*, Jun. 2009, pp. 262–265.

[22] X. Qu, W. Zhang, D. Guo, C. Cai, S. Cai, and Z. Chen, "Iterative thresholding compressed sensing MRI based on contourlet transform," *Inverse Problems Sci. Eng.*, vol. 18, no. 6, pp. 737–758, 2010.

[23] J. Sun, H. Li, and Z. Xu, "Deep ADMM-Net for compressive sensing MRI," in *Proc. Adv. Neural Inf. Process. Syst.*, vol. 29, 2016, pp. 1–9.

[24] X. Qu, Y. Hou, F. Lam, D. Guo, J. Zhong, and Z. Chen, "Magnetic resonance image reconstruction from undersampled measurements using a patch-based nonlocal operator," *Med. Image Anal.*, vol. 18, pp. 843–856, Aug. 2014.

[25] G. Yang, S. Yu, H. Dong, G. Slabaugh, P. L. Dragotti, X. Ye, and F. Liu, "DAGAN: Deep de-aliasing generative adversarial networks for fast compressed sensing MRI reconstruction," *IEEE Trans. Med. Imag.*, vol. 37, no. 6, pp. 1310–1321, Dec. 2017.

[26] D. Liang, J. Cheng, Z. Ke, and L. Ying, "Deep MRI reconstruction: Unrolled optimization algorithms meet neural networks," 2019, *arXiv:1907.11711*.

[27] Y. Wu, Y. Ma, J. Du, and L. Xing, "Accelerating quantitative MR imaging with the incorporation of B_1 compensation using deep learning," *Magn. Reson. Imag.*, vol. 72, pp. 78–86, Oct. 2020.

[28] D. Liang, J. Cheng, Z. Ke, and L. Ying, "Deep magnetic resonance image reconstruction: Inverse problems meet neural networks," *IEEE Signal Process. Mag.*, vol. 37, no. 1, pp. 141–151, Jan. 2020.

[29] D. Lee, J. Yoo, S. Tak, and J. Ye, "Deep residual learning for accelerated MRI using magnitude and phase networks," *IEEE Trans. Biomed. Eng.*, vol. 65, no. 9, pp. 1985–1995, Sep. 2018.

[30] D. Zhao, F. Zhao, and Y. Gan, "Reference-driven compressed sensing MR image reconstruction using deep convolutional neural networks without pre-training," *Sensors*, vol. 20, no. 1, p. 308, Jan. 2020.

[31] V. Singhal and A. Majumdar, "Reconstructing multi-echo magnetic resonance images via structured deep dictionary learning," *Neurocomputing*, vol. 408, pp. 135–143, Sep. 2020.

[32] K. Gong, P. Han, G. El Fakhri, C. Ma, and Q. Li, "Arterial spin labeling MR image denoising and reconstruction using unsupervised deep learning," *NMR Biomed.*, vol. 35, no. 4, p. e4224, Apr. 2022.

[33] A. Majumdar, "An autoencoder based formulation for compressed sensing reconstruction," *Magn. Reson. Imag.*, vol. 52, pp. 62–68, Oct. 2018.

[34] O. Ronneberger, P. Fischer, and T. Brox, "U-Net: Convolutional networks for biomedical image segmentation," in *Proc. Int. Conf. Med. Image Comput. Comput.-Assist. Intervent.*, 2015, pp. 234–241.

[35] Y. Chen, C.-B. Schonlieb, P. Lio, T. Leiner, P. L. Dragotti, G. Wang, D. Rueckert, D. Firmin, and G. Yang, "AI-based reconstruction for fast MRI—A systematic review and meta-analysis," *Proc. IEEE*, vol. 110, no. 2, pp. 224–245, Feb. 2022.

[36] Y. Hou, J. Xu, M. Liu, G. Liu, L. Liu, F. Zhu, and L. Shao, "NLH: A blind pixel-level non-local method for real-world image denoising," *IEEE Trans. Image Process.*, vol. 29, pp. 5121–5135, 2020.

[37] I. Daubechies and W. Sweldens, "Factoring wavelet transforms into lifting steps," *J. Fourier Anal. Appl.*, vol. 4, no. 3, pp. 247–269, 1998.

[38] W. Sweldens, "The lifting scheme: A custom-design construction of biorthogonal wavelets," *Appl. Comput. Harmon. Anal.*, vol. 3, no. 2, pp. 186–200, Apr. 1996.

[39] E. M. Eksioglu and A. K. Tanc, "Denoising AMP for MRI reconstruction: BM3D-AMP-MRI," *SIAM J. Imag. Sci.*, vol. 11, no. 3, pp. 2090–2109, Jan. 2018.

[40] Y. Xie and Q. Li, "Measurement-conditioned denoising diffusion probabilistic model for under-sampled medical image reconstruction," in *Proc. Int. Conf. Med. Image Comput. Comput.-Assist. Intervent.*, 2022, pp. 1–8.

[41] J. Zbontar et al., "FastMRI: An open dataset and benchmarks for accelerated MRI," 2018, *arXiv:1811.08839*.

[42] Z. Wang, A. C. Bovik, H. R. Sheikh, and E. P. Simoncelli, "Image quality assessment: From error visibility to structural similarity," *IEEE Trans. Image Process.*, vol. 13, no. 4, pp. 600–612, Apr. 2004.

[43] A. Buades, B. Coll, and J.-M. Morel, "A non-local algorithm for image denoising," in *Proc. IEEE Comput. Soc. Conf. Comput. Vis. Pattern Recognit. (CVPR)*, Jun. 2005, pp. 60–65.

[44] K. Dabov, A. Foi, V. Katkovnik, and K. Egiazarian, "Image denoising by sparse 3-D transform-domain collaborative filtering," *IEEE Trans. Image Process.*, vol. 16, no. 8, pp. 2080–2095, Aug. 2007.

[45] Y. Hou, C. Zhao, D. Yang, and Y. Cheng, "Comments on 'image denoising by sparse 3-D transform-domain collaborative filtering'," *IEEE Trans. Image Process.*, vol. 20, no. 1, pp. 268–270, Jan. 2011.

HAO HOU received the B.Sc. degree in information and computing science from the School of Mathematical Science, University of Jinan, in 2019. He is currently pursuing the M.Sc. degree with the College of Intelligence and Information Engineering, Shandong University of Traditional Chinese Medicine, Jinan, China. His current research interests include image processing and medical image processing and analysis.

YUCHEN SHAO is currently pursuing the bachelor's degree with the School of Computer Science and Technology, Shandong University, Qingdao, China. His current research interests include image processing and medical image processing and analysis.

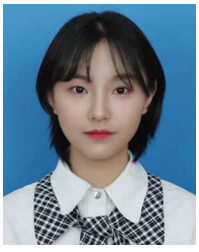

YANG GENG received the B.Sc. degree from the School of Civil Engineering and Architecture, University of Jinan, in 2020. She is currently pursuing the M.Sc. degree with the Qingdao Academy of Chinese Medical Sciences, Shandong University of Traditional Chinese Medicine, Qingdao, China. Her current research interests include image processing and medical image processing and analysis.

YINGKUN HOU (Senior Member, IEEE) received the Ph.D. degree from the School of Computer Science and Technology, Nanjing University of Science and Technology, in 2012. He is currently a Professor with the School of Information Science and Technology, Taishan University, Tai'an, China. His current research interests include image processing, pattern recognition, and artificial intelligence.

PENG DING received the M.D. degree from the School of Software Engineering, East China Normal University, in 2009. He is currently the Deputy Chief Technician with The Second Affiliated Hospital of Shandong University of Traditional Chinese Medicine, Jinan, China. His current research interests include medical health big data and medical image processing and analysis.

BENZHENG WEI received the B.S. degree in computer science from the School of Computer Science, Shandong Institute of Light Industry, Jinan, China, in 2000, the M.S. degree in computer science from the School of Computer Science and Technology, Shandong University, Jinan, in 2007, and the Ph.D. degree in precision instrument and machinery from the College of Automation Engineering, Nanjing University of Aeronautics and Astronautics, Nanjing, China, in 2013. He is currently a Professor with the Shandong University of Traditional Chinese Medicine. He is also acting as the Director of the Center for Medical Artificial Intelligence and the Computational Medicine Laboratory, Shandong University of Traditional Chinese Medicine. He has published more than 80 papers in refereed international leading journals/conferences, such as *Medical Image Analysis*, IEEE TRANSACTIONS ON MEDICAL IMAGING, *Neurocomputing*, IPMI, and MICCAI. His current research interests include artificial intelligence, medical information engineering, and computational medicine.